INTERNATIONAL JOURNAL FOR NUMERICAL METHODS IN FLUIDS
Int. J. Numer. Meth. Fluids **28**: 1109–1134 (1998)

A THREE-DIMENSIONAL HYDRODYNAMIC MODEL IN CURVILINEAR CO-ORDINATES WITH COLLOCATED GRID

JIAN YE[a,*,1], J.A. MCCORQUODALE[b,2] AND R.M. BARRON[c,3]

[a] *Automotive R&D Center, Chrysler Canada Ltd., 3939 Rhodes Drive, P.O. Box 1621, CIMS:242-01-01, Windsor, Ontario, Canada N9A 4H6*
[b] *Department of Civil and Environmental Engineering, University of New Orleans, LA 70148-2210, USA*
[c] *Department of Mathematics and Statistics, and Fluid Dynamics Research Institute, University of Windsor, 401 Sunset Ave., Windsor, Ontario N9B 3P4, Canada*

SUMMARY

A three-dimensional hydrodynamic model has been developed for turbulent flows with free surface. In the horizontal x–y-plane, a boundary-fitted curvilinear co-ordinate system is adopted, while in the vertical direction, a σ-co-ordinate transformation is used to represent the free surface and bed topography or lower boundary. Using the finite volume method, the convection terms are discretized using Roe's second-order-accurate scheme. The governing equations are solved in a collocated grid system by a fractional three-step implicit algorithm that has been developed to handle the velocity–pressure–depth coupling problem of free surface incompressible fluid flows. The present study is the extension of previous work to three-dimensional turbulent flows. The model has been applied to three test cases. Comparison with available data shows that the model developed is successful, and is valuable to engineering application. © 1998 John Wiley & Sons, Ltd.

KEY WORDS: finite volume method; fractional step algorithm; three-dimensional flow; free surface; curvilinear co-ordinates; collocated grid

1. INTRODUCTION

With the rapid development in computer capability, there is an increasing possibility for solving incompressible flows in complex and/or three-dimensional (3D) domains. The nature of the conventional finite difference (FDM) or finite difference based finite volume (FVM) methods makes it difficult for these methods to adequately handle complex boundaries in Cartesian co-ordinates. The boundary-fitted curvilinear co-ordinates technique can be used to extend the applicability of FDM or FVM in CFD [1–3].

Various models have been presented using curvilinear co-ordinate systems, e.g. References [1–5]. These models may vary in one or more aspects, including orthogonal or non-orthogonal co-ordinates, grid systems (staggered or collocated grids), selection of dependent variables in

---

* Correspondence to: Automotive R&D Center, Chrysler Canada Ltd., 3939 Rhodes Drive, P.O. Box 1621, CIMS:242-01-01, Windsor, Ontario, Canada N9A 4H6. Tel: +1 519 2594783; Fax: +1 519 9732895.
[1] E-mail: yejian@server.uwindsor.ca
[2] E-mail: jamce@jazz.uno.edu
[3] E-mail: az3@server.uwindsor.ca

CCC 0271–2091/98/171109–26$17.50

Received 8 February 1996
Revised 10 November 1997

the momentum equations (Cartesian velocities, contravariant or covariant velocity components), discretization methods.

When using curvilinear co-ordinates, it is desirable to use collocated grids, which requires less memory and CPU time [2,5,6]. The momentum interpolation method of Majumdar [6] can be used to suppress the well-known checkerboard non-physical oscillations associated with collocated grid arrangements. This method has shown good stability and accuracy.

Free surface flows commonly occur in hydraulic engineering. Simulation of a free surface flow presents a unique challenge. This is due to the fact that the location of the free surface boundary is unknown and there is no explicit governing equation available to prescribe the movement of a free surface [7]. To reduce this numerical difficulty, the frictionless 'rigid lid' approximation can be used to treat the free surface boundary conditions for most low Froude number ($Fr \ll 1$) flows [8]. For higher Froude number flows with significant variation in elevation from one point to another, three methods (and their variations) have been used: the marker and cell (MAC) method[9]; the fractional volume of fluid (VOF) [7]; and the height function (HF) method [10]. The idea of the MAC method originally proposed by Harlow and Welch [9] is that massless markers moving with the fluid are introduced to define the location and track the movement of the free surface. The VOF method of Hirt and Nichols [7] is based on a finite control volume principle to simulate free surface flow problems. The HF method describes the free surface by the height function [10]. The single-valued nature of the HF method excludes water surface breaking or multi-value free surface problems.

In the present study, a non-orthogonal grid system has been adopted to meet practical requirements in hydraulic engineering. The boundary-fitted co-ordinate transformation has been used in the horizontal x–y-plane to represent the possible irregular boundaries that arise in nature. For the vertical z-co-ordinate, the concept of height function is used to represent the free surface, and the pressure terms in the momentum equations are further decomposed into the sum of a rapidly varying hydrostatic component and the remaining hydrodynamic component, as done by others [10–12]. An algebraic σ-co-ordinate transformation has been constructed in the vertical co-ordinate to track both the bottom topography and free surface [13,14]. The free surface location is updated in the time marching procedure. The Cartesian velocity components are used as dependent variables so that the momentum equations remain in a relatively simple conservative form [2].

Recently, an efficient fractional two-step implicit algorithm was proposed by Ye and Dou [15] to treat the velocity–pressure coupling problem in computations of incompressible fluid flows. Originally, it was developed for simulation of two-dimensional (2D) flows in Cartesian co-ordinates with staggered grids. Later, this algorithm was modified to apply to curvilinear co-ordinates with a collocated grid arrangement to 2D flows [5] and 2D depth-averaged flows [16]. Based on the fractional step principles, the proposed procedures involve implementation of two steps: Step 1 is the convection–diffusion process; Step 2 is the pressure propagation process [5,15,16]. In this paper, the previous fractional two-step implicit algorithm has been extended to a fractional three-step implicit algorithm to handle the velocity–pressure–depth coupling problem for 3D flows with free surface. Step 1 is the convection–diffusion process; Step 2 is the hydrostatic pressure propagation process and Step 3 is the hydrodynamic propagation step. The FVM is applied to the time discretized form of the transport equations.

To overcome the problem of numerical diffusion associated with first-order upwind schemes, e.g. hybrid and power law schemes, the second-order upwind scheme of Roe [17] has been incorporated into the code to discretize the convection terms. Roe's scheme has been applied extensively in aerodynamics [18–20] and hydrodynamics with shockwave-type flows [21], because of its outstanding performance in hyperbolic problems and its relatively simple form

[20]. Recently, Roe's scheme has been applied to the convection–diffusion transport equations [5,16]. Applications have shown that Roe's scheme meets the requirements of high accuracy and computational efficiency [5,16,20,21].

The objective of this paper is to report the development of the fractional three-step solution procedure for the computation of 3D turbulent flows with a free surface in boundary-fitted curvilinear collocated grids. The applicability of the proposed model is demonstrated through three test cases. The standard k–ϵ turbulence model [22,23] has been used to estimate the turbulent viscosity.

2. GOVERNING EQUATIONS

2.1. Governing equations in Cartesian co-ordinates

For a 3D turbulent flow of an incompressible Newtonian fluid with the Boussinesq eddy viscosity approximation, the unsteady governing equations in (x, y, z) Cartesian co-ordinates are:
Continuity equation

$$\frac{\partial u}{\partial x}+\frac{\partial v}{\partial y}+\frac{\partial w}{\partial z}=0. \tag{1}$$

Momentum equations

$$\frac{\partial \phi}{\partial T}+\frac{\partial u\phi}{\partial x}+\frac{\partial v\phi}{\partial y}+\frac{\partial w\phi}{\partial z}=\frac{\partial}{\partial x}\left(v_e\frac{\partial \phi}{\partial x}\right)+\frac{\partial}{\partial y}\left(v_e\frac{\partial \phi}{\partial y}\right)+\frac{\partial}{\partial z}\left(v_e\frac{\partial \phi}{\partial z}\right)+S^*_\phi, \tag{2}$$

in which

$$\phi=u, \qquad S^*_u=-\frac{\partial P}{\partial x}, \tag{3a}$$

$$\phi=v, \qquad S^*_v=-\frac{\partial P}{\partial y}, \tag{3b}$$

$$\phi=w, \qquad S^*_w=-\frac{\partial P}{\partial z}-g. \tag{3c}$$

Here u, v, w are the velocity components in the horizontal x-, y- and vertical z-directions respectively, g is the acceleration due to gravity, $v_e=v_t+v$, v_t is the turbulent viscosity, v is the fluid kinematic viscosity, P is the kinetic pressure (pressure divided by fluid density) and T is time.

The moving free surface is represented by $z=H+Z_b$, where H is the variable water depth and Z_b is the bed elevation. The total pressure P at any position (x, y, z) can be subdivided into (a) the hydrostatic component, i.e. $P_0+g(H+Z_b-z)$, where P_0 is the free surface kinetic pressure, and (b) the residual hydrodynamic component p, i.e. $p=P-P_0-g(H+Z_b-z)$.

2.2. Governing equations in curvilinear co-ordinates

In the x–y-plane, a boundary-fitted co-ordinate system (ξ, η) is introduced to represent the natural irregular geometry: $\xi=\xi(x, y)$, $\eta=\eta(x, y)$, $t(T)=T$. In the vertical (z-direction), a σ-co-ordinate is defined as

$$\sigma(x, y, z, T) = \frac{H(x, y, T) + Z_b(x, y) - z}{H(x, y, T)}. \tag{4}$$

Since the flow region is restricted by $Z_b < z \le H + Z_b$, Equation (4) implies $0 \le \sigma \le 1$. Figure 1 shows the curvilinear co-ordinate system used. The σ-transformation (4) is an economical way to represent the movement of a singe-valued free surface [13,14]. In the computational co-ordinates, $\sigma \equiv 0$ corresponds to the water surface ($z = H + Z_b$), while $\sigma \equiv 1$ is the bottom ($z = Z_b$). In the new co-ordinate system, the velocities are defined as

$$U = uy_\eta - vx_\eta, \qquad V = vx_\xi - uy_\xi, \tag{5}$$

$$W = \frac{D\sigma}{DT} = \frac{\partial\sigma}{\partial T} + u\frac{\partial\sigma}{\partial x} + v\frac{\partial\sigma}{\partial y} + w\frac{\partial\sigma}{\partial z} = \frac{1}{H}\left[(1-\sigma)\frac{\partial H}{\partial t} + \frac{1}{J}(Uz_\xi + Vz_\eta) - w\right], \tag{6}$$

where U, V are called the contravariant velocities which are perpendicular to the curvilinear co-ordinates η and ξ respectively.

By the chain rule, the governing equations in these non-orthogonal curvilinear co-ordinates, using Cartesian velocities (represented by ϕ) as dependent variables in the momentum equations, can be stated as

Continuity equation

$$\frac{\partial HJ}{\partial t} + \frac{\partial HU}{\partial \xi} + \frac{\partial HV}{\partial \eta} + \frac{\partial HJW}{\partial \sigma} = 0. \tag{7}$$

Momentum equations

$$\begin{aligned}
&\frac{\partial HJ\phi}{\partial t} + \frac{\partial HU\phi}{\partial \xi} + \frac{\partial HV\phi}{\partial \eta} + \frac{\partial HJW\phi}{\partial \sigma} \\
&= \frac{\partial}{\partial \xi}\left[\frac{Hv_e}{J}\left(\alpha\phi_\xi - \beta\phi_\eta + \frac{q_{13}}{H}\phi_\sigma\right)\right] + \frac{\partial}{\partial \eta}\left[\frac{Hv_e}{J}\left(\gamma\phi_\eta - \beta\phi_\xi + \frac{q_{23}}{H}\phi_\sigma\right)\right] \\
&\quad + \frac{\partial}{\partial \sigma}\left[\frac{v_e}{J}\left(q_{31}\phi_\xi + q_{32}\phi_\eta + \frac{q_{33}}{H}\phi_\sigma\right)\right] + S_\phi,
\end{aligned} \tag{8}$$

where

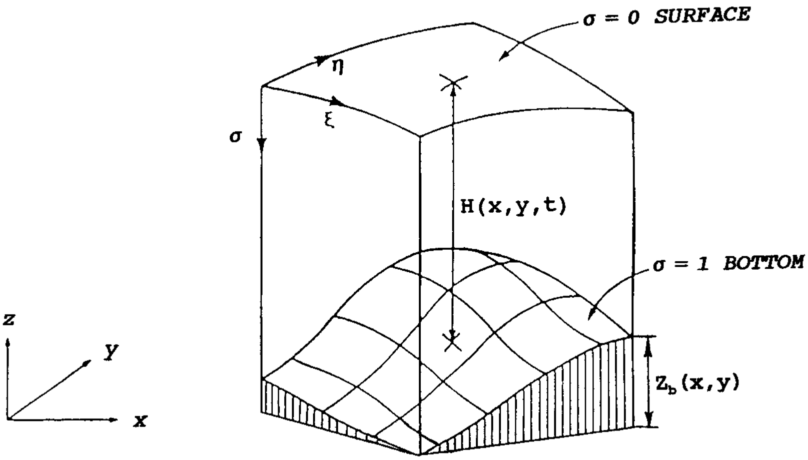

Figure 1. Co-ordinate system.

$$\alpha = x_\eta^2 + y_\eta^2, \qquad \beta = x_\xi x_\eta + y_\xi y_\eta, \qquad \gamma = x_\xi^2 + y_\xi^2, \qquad J = x_\xi y_\eta - x_\eta y_\xi,$$
$$q_{31} = q_{13} = \alpha z_\xi - \beta z_\eta, \qquad q_{32} = q_{23} = \gamma z_\eta - \beta z_\xi,$$
$$q_{33} = (y_\xi z_\eta - y_\eta z_\xi)^2 + (x_\xi z_\eta - x_\eta z_\xi)^2 + J^2, \qquad z(\xi, \eta, \sigma, t) = H + Z_\mathrm{b} - \sigma H. \tag{9}$$

The source terms S_ϕ are given by

$$\phi = u: \quad S_u = -H\left\{y_\eta \frac{\partial}{\partial \xi}[g(H+Z_\mathrm{b})+p] - y_\xi \frac{\partial}{\partial \eta}[g(H+Z_\mathrm{b})+p]\right\} - \frac{\partial p}{\partial \sigma}(y_\eta z_\xi - y_\xi z_\eta), \tag{10}$$

$$\phi = v: \quad S_v = -H\left\{x_\xi \frac{\partial}{\partial \eta}[g(H+Z_\mathrm{b})+p] - x_\eta \frac{\partial}{\partial \xi}[g(H+Z_\mathrm{b})+p]\right\} - \frac{\partial p}{\partial \sigma}(x_\xi z_\eta - x_\eta z_\xi), \tag{11}$$

$$\phi = w: \quad S_w = J\frac{\partial p}{\partial \sigma}. \tag{12}$$

Integrating Equation (7) over the depth leads to the following equation for determining the location of free surface [11,12]:

$$\frac{\partial HJ}{\partial t} + \frac{\partial H\bar{U}}{\partial \xi} + \frac{\partial H\bar{V}}{\partial \eta} = 0, \tag{13}$$

where the overbars denote the depth-averaged values. The standard k–ϵ model [22,23] has been employed to determine ν_t in the momentum equation (8).

3. NUMERICAL PROCEDURE

3.1. The fractional three-step implicit algorithm

Based on the split-operator approach for the different transport processes [24,25], the numerical procedure of the fractional two-step implicit algorithm proposed by Ye *et al.* [5,15,16] is divided into the following two steps: Step 1 is the convection–diffusion process and Step 2 is the propagation process. In this paper, Step 2 is further subdivided into the hydrostatic and hydrodynamic propagation processes. The framework of the proposed fractional three-step implicit algorithm is as follows:

Step 1: Convection–diffusion process $\Rightarrow u^{n+1/3}, v^{n+1/3}, w^{n+1/3}$;
Step 2: Hydrostatic propagation process $\Rightarrow H^{n+1}, u^{n+2/3}, v^{n+2/3}, w^{n+2/3}$;
Step 3: Hydrodynamic propagation process $\Rightarrow p^{n+1}, u^{n+1}, v^{n+1}, w^{n+1}$;

The superscript $n+1$ refers to the time level $(n+1)\Delta t$ etc., while the superscripts $n+1/3$, $n+2/3$ denote the intermediate variables between steps. The following primed quantities are defined for convenience: $[(u, v, w) = (u_1, u_2, u_3), (U, V, W) = (U_1, U_2, U_3)]$

$$u_i' = u_i^{n+2/3} - u_i^{n+1/3}, \qquad U_i' = U_i^{n+2/3} - U_i^{n+1/3}, \qquad u_i'' = u_i^{n+1} - u_i^{n+2/3},$$
$$U_i'' = U_i^{n+1} - U_i^{n+2/3}, \qquad H' = H^{n+1} - H^n, \qquad p' = p^{n+1} - p^n, \quad (i = 1, 2, 3). \tag{14}$$

In the propagation steps, a coefficient of implicitization Π is introduced for spatial derivatives to accelerate the rate of convergence to a steady state [15,24], e.g. for ξ-direction,

$$\frac{\partial(H+Z_{\mathrm{b}})}{\partial\xi}=\left(\frac{\partial(H+Z_{\mathrm{b}})}{\partial\xi}\right)^{n}+\Pi\,\frac{\partial H'}{\partial\xi};\qquad \frac{\partial H\bar{U}_j}{\partial\xi}=\Pi\left(\frac{\partial H\bar{U}_j}{\partial\xi}\right)^{n+2/3}+(1-\Pi)\left(\frac{\partial H\bar{U}_j}{\partial\xi}\right)^{n+1/3};$$
$$\frac{\partial p}{\partial\xi}=\left(\frac{\partial p}{\partial\xi}\right)^{n}+\Pi\,\frac{\partial p'}{\partial\xi};\qquad \frac{\partial HU_j}{\partial\xi}=\Pi\left(\frac{\partial HU_j}{\partial\xi}\right)^{n+1}+(1-\Pi)\left(\frac{\partial HU_j}{\partial\xi}\right)^{n+2/3}. \tag{15}$$

In practice, the known values of the pressure gradient in the momentum equations at the time level $n\Delta t$ are substituted explicitly in Step 1 as source terms; the remainder of which, i.e. terms $\partial H'/\partial\xi$ and $\partial p'/\partial\xi$ etc., combined with the depth-averaged form of continuity equation (13) and the continuity equation (7) are evaluated in Steps 2 and 3, respectively. Thus, the working equations of the fractional three-step algorithm, are

Step 1: Convection–diffusion process

$$J\,\frac{(H\phi)^{n+1/3}-(H\phi)^{n}}{\Delta t}+[(HU)^{n}\phi^{n+1/3}]_{\xi}+[(HV)^{n}\phi^{n+1/3}]_{\eta}+J[(HW)^{n}\phi^{n+1/3}]_{\sigma}$$
$$=\left[\frac{v_eH^n}{J}\left(\alpha\phi_{\xi}^{n+1/3}-\beta\phi_{\eta}^{n}+\frac{q_{13}}{H^n}\,\phi_{\sigma}^{n}\right)\right]_{\xi}+\left[\frac{v_eH^n}{J}\left(\gamma\phi_{\eta}^{n+1/3}-\beta\phi_{\xi}^{n}+\frac{q_{23}}{H^n}\,\phi_{\sigma}^{n}\right)\right]_{\eta}$$
$$+\left[\frac{v_e}{J}\left(q_{31}\phi_{\xi}^{n}+q_{32}\phi_{\eta}^{n}+\frac{q_{33}}{H^n}\,\phi_{\sigma}^{n+1/3}\right)\right]_{\sigma}+S_{\phi}^{n}, \tag{16}$$

where $H^{n+1/3}=H^{n}$. The expressions for the source terms S_{ϕ} of the momentum equations can be found in Equations (10)–(12).

Step 2: Hydrostatic propagation process ($w^{n+2/3}=w^{n+1/3}$)

$$\frac{(Hu)^{n+2/3}-(Hu)^{n+1/3}}{\Delta t}=-\Pi\,\frac{gH^n}{J}\left(\frac{\partial H'}{\partial\xi}\,y_{\eta}-\frac{\partial H'}{\partial\eta}\,y_{\xi}\right), \tag{17a}$$

$$\frac{(Hv)^{n+2/3}-(Hv)^{n+1/3}}{\Delta t}=-\Pi\,\frac{gH^n}{J}\left(\frac{\partial H'}{\partial\eta}\,x_{\xi}-\frac{\partial H'}{\partial\xi}\,x_{\eta}\right), \tag{17b}$$

$$J\,\frac{H^{n+2/3}-H^{n+1/3}}{\Delta t}+\left(\frac{\partial(H\bar{U})^{n+1/3}}{\partial\xi}+\frac{\partial(H\bar{V})^{n+1/3}}{\partial\eta}\right)+\Pi\left(\frac{\partial H\bar{U}'}{\partial\xi}+\frac{\partial H\bar{V}'}{\partial\eta}\right)=0. \tag{17c}$$

Step 3: Hydrodynamic propagation process ($H^{n+1}=H^{n+2/3}$)

$$\frac{(Hu)^{n+1}-(Hu)^{n+2/3}}{\Delta t}=-\Pi\,\frac{H^{n+1}}{J}\left(\frac{\partial p'}{\partial\xi}\,y_{\eta}-\frac{\partial p'}{\partial\eta}\,y_{\xi}\right)-\Pi\,\frac{1}{J}\,\frac{\partial p'}{\partial\sigma}\,(y_{\eta}z_{\xi}-y_{\xi}z_{\eta}), \tag{18a}$$

$$\frac{(Hv)^{n+1}-(Hv)^{n+2/3}}{\Delta t}=-\Pi\,\frac{H^{n+1}}{J}\left(\frac{\partial p'}{\partial\eta}\,x_{\xi}-\frac{\partial p'}{\partial\xi}\,x_{\eta}\right)-\Pi\,\frac{1}{J}\,\frac{\partial p'}{\partial\sigma}\,(x_{\xi}z_{\eta}-x_{\eta}z_{\xi}), \tag{18b}$$

$$\frac{(Hw)^{n+1}-(Hw)^{n+2/3}}{\Delta t}=\Pi\,\frac{\partial p'}{\partial\sigma}, \tag{18c}$$

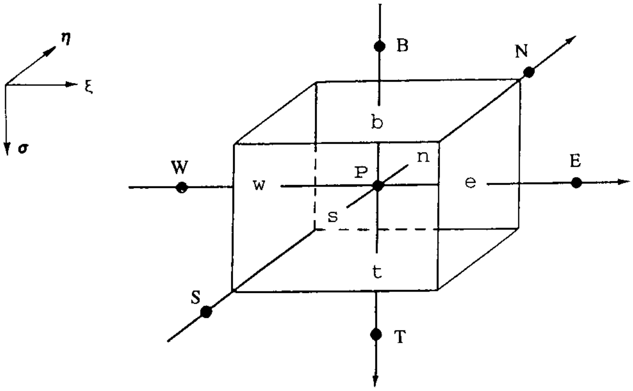

Figure 2. Typical control volume for node P.

$$J\frac{H^{n+1}-H^{n+2/3}}{\Delta t}+\frac{\partial(HU)^{n+2/3}}{\partial\xi}+\frac{\partial(HV)^{n+2/3}}{\partial\eta}+J\frac{\partial(HW)^{n+2/3}}{\partial\sigma}$$

$$+\Pi\left(\frac{\partial HU''}{\partial\xi}+\frac{\partial HV''}{\partial\eta}+J\frac{\partial HW''}{\partial\sigma}\right)=0. \qquad (18d)$$

3.2. Numerical discretization

The working equations of each step are discretized in space by using the FVM. The notation system of Patankar [26] has been adopted throughout the following derivation. A typical control volume for node P is shown in Figure 2, where the capital letters E, N, T, etc. denote the neighbouring nodes and the small letters e, n, t, etc. denote the control volume faces.

In Step 1, the general form of convection–diffusion equation (16) is integrated over a typical control volume $\Delta\xi\ \Delta\eta\ \Delta\sigma$ of node P. All the spatial derivatives are estimated with second-order-accurate central difference, except for the convection terms whose face values represented in terms of nodal values can be obtained by a variety of upwind schemes. Various monotonic schemes are available to reduce the numerical diffusion and provide stable solutions [17–20,27]. This work uses Roe's scheme [17,18] to discretize the convective fluxes because of its good performance in shock-capture and high computational efficiency. The principle of Roe's scheme is that resolutions of the first-order upwind scheme can be improved by adding high-order (antidiffusion) terms that are limited to ensure monotonic results [27]. For example, in a uniform grid system at e face, the resulting monotonic second-order upwind scheme of Roe for the convection flux $HU\phi$ is written as [19,20]

$$(HU\phi)_{\mathrm{e}}=[\![F_{\mathrm{e}},0]\!](\phi_{\mathrm{P}}+\Omega_{\mathrm{e}}^{-}\ \Delta\phi_{\mathrm{e}}^{-})-[\![-F_{\mathrm{e}},0]\!](\phi_{\mathrm{E}}-\Omega_{\mathrm{e}}^{+}\ \Delta\phi_{\mathrm{e}}^{+}), \qquad (19)$$

where

$$\Delta\phi_{\mathrm{e}}^{-}=(\phi_{\mathrm{P}}-\phi_{\mathrm{W}})*0.5; \qquad \Delta\phi_{\mathrm{e}}^{+}=(\phi_{\mathrm{EE}}-\phi_{\mathrm{E}})*0.5, \qquad (20)$$

$$\Omega_{\mathrm{e}}^{\mp}=[\![0,\min(2r_{\mathrm{e}}^{\mp},1),\min(r_{\mathrm{e}}^{\mp},2)]\!], \qquad (21)$$

$$r_{\mathrm{e}}^{-}=(\phi_{\mathrm{E}}-\phi_{\mathrm{P}})/(\phi_{\mathrm{P}}-\phi_{\mathrm{W}}); \qquad r_{\mathrm{e}}^{+}=(\phi_{\mathrm{P}}-\phi_{\mathrm{E}})/(\phi_{\mathrm{E}}-\phi_{\mathrm{EE}}), \qquad (22)$$

and $F_{\mathrm{e}}=(HU)_{\mathrm{e}}$, r_{e} is the ratio of consecutive gradients, and Ω_{e} is the flux limiter that corresponds to Roe's 'superbee' compressive transfer function.

The final discretized form of Equation (16) ($\Delta\xi=\Delta\eta=1$) is

$$a_{\rm p}\phi_{\rm P}^{n+1/3} = \sum a_{\rm nb}\phi_{\rm nb}^{n+1/3} + b + a_{\rm P}^{*}\phi^{n} + S_{\phi}. \tag{23}$$

The coefficients of Equation (23) can be written in the compact format

$$a_I = D_i A(|P_i|) + [\![-F_i, 0]\!] \quad (\text{where } I = \text{E, N, T}, \ldots, \quad i = \text{e, n, t}, \ldots),$$

$$b = \left[\frac{\Gamma_\phi H^n}{J}\left(-\beta\phi_\eta^n + \frac{q_{13}}{H^n}\phi_\sigma^n\right)\right]\Bigg|_{\rm w}^{\rm e} + \left[\frac{\Gamma_\phi H^n}{J}\left(-\beta\phi_\xi^n + \frac{q_{23}}{H^n}\phi_\sigma^n\right)\right]\Bigg|_{\rm s}^{\rm n}$$
$$+ \left[\frac{\Gamma_\phi}{J}\left(q_{31}\phi_\xi^n + q_{32}\phi_\eta^n\right)\right]\Bigg|_{\rm b}^{\rm t}/\Delta\sigma + B_{\rm anti},$$

$$a_{\rm p} = \sum a_{\rm nb} + a_{\rm P}^{*}, \qquad a_{\rm P}^{*} = H^n J/\Delta t, \qquad P_i = F_i/D_i,$$

$$F_{\rm e} = (HU)_{\rm e}^{\rm n}, \qquad F_{\rm w} = (HU)_{\rm w}^{\rm n}, \qquad F_{\rm n} = (HV)_{\rm n}^{n}, \qquad F_{\rm s} = (HV)_{\rm s}^{n}, \qquad F_{\rm t} = (HW)_{\rm t}^{n}J/\Delta\sigma,$$
$$F_{\rm b} = (HW)_{\rm b}^{n}J/\Delta\sigma, \qquad D_{\rm e} = (\alpha v_e H^n/J)_{\rm e}/\delta\xi_{\rm e}, \qquad D_{\rm w} = (\alpha v_e H^n/J)_{\rm w}/\delta\xi_{\rm w},$$
$$D_{\rm n} = (\gamma v_e H^n/J)_{\rm n}/\delta\eta_{\rm n}, \qquad D_{\rm s} = (\gamma v_e H^n/J)_{\rm s}/\delta\eta_{\rm s},$$
$$D_{\rm t} = (v_e q_{33})_{\rm t}/(JH^n\Delta\sigma\delta\sigma_{\rm t}), \qquad D_{\rm b} = (v_e q_{33})_{\rm b}/(JH^n\Delta\sigma\delta\sigma_{\rm b}),$$

For Roe's scheme:

$$A(|P|) \equiv 1, \tag{24}$$

$$B_{\rm anti} = [\![F_{\rm w}, 0]\!]\Omega_{\rm w}^{-}\Delta\phi_{\rm w}^{-} + [\![-F_{\rm w}, 0]\!]\Omega_{\rm w}^{+}\Delta\phi_{\rm w}^{+} - [\![F_{\rm e}, 0]\!]\Omega_{\rm e}^{-}\Delta\phi_{\rm e}^{-} - [\![-F_{\rm e}, 0]\!]\Omega_{\rm e}^{+}\Delta\phi_{\rm e}^{+}$$
$$+ [\![F_{\rm s}, 0]\!]\Omega_{\rm s}^{-}\Delta\phi_{\rm s}^{-} + [\![-F_{\rm s}, 0]\!]\Omega_{\rm s}^{+}\Delta\phi_{\rm s}^{+} - [\![F_{\rm n}, 0]\!]\Omega_{\rm n}^{-}\Delta\phi_{\rm n}^{-} - [\![-F_{\rm n}, 0]\!]\Omega_{\rm n}^{+}\Delta\phi_{\rm n}^{+}$$
$$+ [\![F_{\rm b}, 0]\!]\Omega_{\rm b}^{-}\Delta\phi_{\rm b}^{-} + [\![-F_{\rm b}, 0]\!]\Omega_{\rm b}^{+}\Delta\phi_{\rm b}^{+} - [\![F_{\rm t}, 0]\!]\Omega_{\rm t}^{-}\Delta\phi_{\rm t}^{-} - [\![-F_{\rm t}, 0]\!]\Omega_{\rm t}^{+}\Delta\phi_{\rm n}^{+},$$

where Ω_i and $\Delta\phi_i$ are defined in Equations (20) and (21). If the power law scheme [26] is considered, the above terms should be replaced by

$$A(|P|) = [\![0, (1 - 0.1|P|)^5]\!], \qquad B_{\rm anti} \equiv 0. \tag{25}$$

For 3D computations, it is obvious that Roe's scheme leads to a 13-point stencil and the power law approximation corresponds to a seven-point stencil. Thus, the momentum equations are discretized as

u-momentum equation

$$a_{\rm P}u_{\rm P}^{n+1/3} = \sum a_{\rm nb}u_{\rm nb}^{n+1/3} + b^u + a_{\rm P}^{*}u_{\rm P}^{n} + B^u\frac{\partial}{\partial\xi}[g(H + Z_{\rm b})^n + p^n] + C^u\frac{\partial}{\partial\eta}[g(H + Z_{\rm b})^n + p^n]$$
$$+ D^u\frac{\partial p^n}{\partial\sigma}, \tag{26}$$

where

$$B^u = -y_\eta H^n, \qquad C^u = y_\xi H^n, \qquad D^u = (y_\xi z_\eta - y_\eta z_\xi).$$

v-momentum equation

$$a_{\mathrm{P}}v_{\mathrm{P}}^{n+1/3}=\sum a_{\mathrm{nb}}v_{\mathrm{nb}}^{n+1/3}+b^{v}+a_{\mathrm{P}}^{*}v_{\mathrm{P}}^{n}+B^{v}\frac{\partial}{\partial\xi}\left[g(H+Z_{\mathrm{b}})^{n}+p^{n}\right]+C^{v}\frac{\partial}{\partial\eta}\left[g(H+Z_{\mathrm{b}})^{n}+p^{n}\right]$$
$$+D^{v}\frac{\partial p^{n}}{\partial\sigma}, \tag{27}$$

where

$$B^{v}=x_{\eta}H^{n},\qquad C^{v}=-x_{\xi}H^{n},\qquad D^{v}=(x_{\eta}z_{\xi}-x_{\xi}z_{\eta}).$$

w-momentum equation

$$a_{\mathrm{P}}w_{\mathrm{P}}^{n+1/3}=\sum a_{\mathrm{nb}}w_{\mathrm{nb}}^{n+1/3}+b^{w}+a_{\mathrm{P}}^{*}w_{\mathrm{P}}^{n}+J\frac{\partial p^{n}}{\partial\sigma}. \tag{28}$$

In Step 2, omitting the higher order magnitude of products Hu, Hv in Equation (17a,b) and integrating u', v' over the depth, one can obtain U', V' as

$$U'=\bar{U}'=\frac{y_{\eta}}{H}\int_{Z_{\mathrm{b}}}^{H+Z_{\mathrm{b}}}\bar{u}'\,\mathrm{d}z-\frac{x_{\eta}}{H}\int_{Z_{\mathrm{b}}}^{H+Z_{\mathrm{b}}}\bar{v}'\,\mathrm{d}z=-\alpha gd\frac{\partial H'}{\partial\xi}+\beta gd\frac{\partial H'}{\partial\eta}, \tag{29}$$

$$V'=\bar{V}'=\frac{x_{\xi}}{H}\int_{Z_{\mathrm{b}}}^{H+Z_{\mathrm{b}}}\bar{v}'\,\mathrm{d}z-\frac{y_{\xi}}{H}\int_{Z_{\mathrm{b}}}^{H+Z_{\mathrm{b}}}\bar{u}'\,\mathrm{d}z=-\gamma gd\frac{\partial H'}{\partial\eta}+\beta gd\frac{\partial H'}{\partial\xi}, \tag{30}$$

where $d=\Pi\Delta t/J$. The above relations can be applied to any point, i.e. either at a grid node or on a control volume face. To simplify the water depth correction equation, and retain the five-point diagonal equation set, the last term on the right-hand side of Equations (29) and (30) can be dropped without affecting the final converged results. Thus

$$\bar{U}'\approx-\bar{B}H'_{\xi},\qquad\bar{V}'\approx-\bar{C}H'_{\eta};\qquad\bar{B}=\alpha gd,\qquad\bar{C}=\gamma gd. \tag{31}$$

Substituting Equation (31) into (17c), and integrating over the control volume $\Delta\xi\ \Delta\eta$, the final water depth correction equation is

$$\bar{A}_{\mathrm{P}}H'_{\mathrm{P}}=\sum\bar{A}_{\mathrm{nb}}H'_{\mathrm{nb}}+\bar{E}, \tag{32}$$

where

$$\bar{A}_{\mathrm{E}}=\Pi(H^{n}\bar{B})_{\mathrm{e}},\qquad\bar{A}_{\mathrm{W}}=\Pi(H^{n}\bar{B})_{\mathrm{w}},\qquad\bar{A}_{\mathrm{N}}=\Pi(H^{n}\bar{C})_{\mathrm{n}},\qquad\bar{A}_{\mathrm{S}}=\Pi(H^{n}\bar{C})_{\mathrm{s}},$$

$$\bar{A}_{\mathrm{P}}=\sum\bar{A}_{\mathrm{nb}}+J/\Delta t,\qquad\bar{E}=[(H\bar{U})_{\mathrm{w}}^{n+1/3}-(H\bar{U})_{\mathrm{e}}^{n+1/3}]+[(H\bar{V})_{\mathrm{s}}^{n+1/3}-(H\bar{V})_{\mathrm{n}}^{n+1/3}].$$

In Step 3, U'',V'',W'' are obtained from Equation (18a–c):

$$U''=u''y_{\eta}-v''x_{\eta}=-B\frac{\partial p'}{\partial\xi}+\beta d\frac{\partial p'}{\partial\eta}-d\frac{\alpha z_{\xi}-\beta z_{\eta}}{J}\frac{\partial p'}{\partial\sigma},$$

$$V''=v''x_{\xi}-u''y_{\xi}=\beta d\frac{\partial p'}{\partial\xi}-C\frac{\partial p'}{\partial\eta}-d\frac{\gamma z_{\eta}-\beta z_{\xi}}{J}\frac{\partial p'}{\partial\sigma},$$

$$W''=\frac{1}{HJ}(U''z_{\xi}+V''z_{\eta})-\frac{w''}{H}=-d\frac{\alpha z_{\xi}-\beta z_{\eta}}{HJ}\frac{\partial p'}{\partial\xi}-d\frac{\gamma z_{\eta}-\beta z_{\xi}}{HJ}\frac{\partial p'}{\partial\eta}-D\frac{\partial p}{\partial\sigma},$$

where

$$B=\alpha d, \qquad C=\gamma d, \qquad D=\frac{d}{H^2}\left[\frac{\alpha z_\xi^2+\gamma z_\eta^2-2\beta z_\xi z_\eta}{J}+J\right].$$

The above correction equations are simplified further as

$$U''\approx -B\frac{\partial p'}{\partial \xi}, \qquad V''\approx -C\frac{\partial p'}{\partial \eta}, \qquad W''\approx -D\frac{\partial p'}{\partial \sigma}. \tag{33}$$

Substituting Equation (33) into (18d), the final hydrodynamic pressure correction equation is

$$A_{\mathrm{P}}p'_{\mathrm{P}}=\sum A_{\mathrm{nb}}p'_{\mathrm{nb}}+E, \tag{34}$$

where

$$A_{\mathrm{E}}=\Pi(H^{n+1}B)_{\mathrm{e}}, \qquad A_{\mathrm{W}}=\Pi(H^{n+1}B)_{\mathrm{w}}, \qquad A_{\mathrm{N}}=\Pi(H^{n+1}C)_{\mathrm{n}}, \qquad A_{\mathrm{S}}=\Pi(H^{n+1}C)_{\mathrm{s}},$$

$$A_{\mathrm{T}}=\Pi(D)_{\mathrm{t}}\,JH^{n+1}/\Delta\sigma, \qquad A_{\mathrm{B}}=\Pi(D)_{\mathrm{b}}\,JH^{n+1}/\Delta\sigma,$$

$$A_{\mathrm{P}}=\sum A_{\mathrm{nb}}+J/\Delta t, \qquad E=(HU)^{n+2/3}\big|_{\mathrm{e}}^{\mathrm{w}}+(HV)^{n+2/3}\big|_{\mathrm{n}}^{\mathrm{s}}+(HW)^{n+2/3}\big|_{\mathrm{t}}^{\mathrm{b}}J/\Delta\sigma.$$

Step 2, the hydrostatic propagation process, and Step 3, the hydrodynamic propagation process, of the proposed algorithm resemble the velocity–pressure correction procedure in the SIMPLE-like algorithm [5,28], and the derivation of the velocity and pressure (water depth) correction equations (31)–(34) is straightforward.

3.3. *Pressure–velocity coupling*

Since collocated grids are used, interpolation is needed to estimate the convective flux at the control volume faces, e.g. $U_{\mathrm{e}}^{n+2/3}$, $V_{\mathrm{n}}^{n+2/3}$, $W_{\mathrm{t}}^{n+2/3}$, in the source term E of Equation (34). To avoid the non-physical checkerboard oscillations, the revised momentum interpolation procedure of Majumdar [6] is adopted because the converged solution of this method is independent of the relaxation parameter (or time step Δt in the unsteady approach). For example, values of U at the e cell face can be expressed as

$$\begin{aligned}U_{\mathrm{e}}^{n+2/3}={}&\overline{\langle U_{\mathrm{P}}^{n+2/3}\rangle}_{\mathrm{e}}+\left\langle\overline{\frac{a_{\mathrm{p}}^*}{a_{\mathrm{P}}}}\right\rangle_{\mathrm{e}}U_{\mathrm{e}}^n-\left\langle\overline{\frac{a_{\mathrm{p}}^*}{a_{\mathrm{P}}}U_{\mathrm{P}}^n}\right\rangle_{\mathrm{e}}+\left\langle\overline{\frac{B^u}{a_{\mathrm{P}}}y_\eta-\frac{B^v}{a_{\mathrm{P}}}x_\eta}\right\rangle_{\mathrm{e}}\left(\frac{\partial(PP)^n}{\partial\xi}\right)_{\mathrm{e}}\\&-\left\langle\overline{\left(\frac{B^u}{a_{\mathrm{P}}}y_\eta-\frac{B^v}{a_{\mathrm{P}}}x_\eta\right)\left(\frac{\partial(PP)^n}{\partial\xi}\right)_{\mathrm{p}}}\right\rangle_{\mathrm{e}},\end{aligned} \tag{35}$$

where $PP=g(H+Z_{\mathrm{b}})+p$. The expression for V at the north cell face can be derived similarly.

From Equation (6), the velocity W at the top cell face is

$$W_{\mathrm{t}}^{n+2/3}=\langle\overline{W_{\mathrm{P}}^{n+2/3}}\rangle_{\mathrm{t}}\left\langle\overline{\frac{a_{\mathrm{P}}^*}{a_{\mathrm{P}}}}\right\rangle_{\mathrm{t}}W_{\mathrm{t}}^n-\left\langle\overline{\frac{a_{\mathrm{P}}^*}{a_{\mathrm{P}}}W_{\mathrm{P}}^n}\right\rangle_{\mathrm{t}}+\langle\overline{DD_{\mathrm{P}}}\rangle_{\mathrm{t}}\left(\frac{\partial p^n}{\partial\sigma}\right)_{\mathrm{t}}-\left\langle\overline{DD_{\mathrm{P}}\left(\frac{\partial p^n}{\partial\sigma}\right)_{\mathrm{P}}}\right\rangle_{\mathrm{t}}, \tag{36}$$

where

$$DD_{\mathrm{P}}=\frac{1}{a_{\mathrm{P}}H_{\mathrm{P}}^n}\left[\frac{D^u}{J}(y_\eta z_\xi-y_\xi z_\eta)+\frac{D^v}{J}(x_\xi z_\eta-x_\eta z_\xi)-J\right].$$

The expressions of B^u, D^u, etc. are given in Equations (26)–(28). The same procedure is applied to the water depth correction equation (32).

3.4. Solution procedure

The overall numerical procedure can be summarized as follows:

(I) Use the known values of u^n, v^n, w^n, $(H+Z_b)^n$, p^n at time $n\Delta t$ to evaluate the coefficients of the convection–diffusion equation (23) and obtain velocities $u^{n+1/3}$ etc. through Equations (26)–(28) at the grid nodes (to complete Step 1).
(II) Interpolate $U^{n+1/3}$ etc. onto the cell faces.
(III) Solve Equation (32) for H' and $(H+Z_b)^{n+1}$, then obtain $U^{n+2/3}$, $V^{n+2/3}$ and $u^{n+2/3}$, $v^{n+2/3}$ according Equations (31) and (5) (to complete Step 2).
(IV) Solve Equation (34) for p′ and p^{n+1}, and obtain U^{n+1}, u^{n+1} etc. using Equations (33), (5) and (6) (to complete Step 3).
(V) Solve the discretized transport equations for other scalar variables, such as k, ϵ to complete the current time step.
(VI) Return to I and march to the next time step.
(VII) Repeat the entire procedure until a steady-state solution is reached (for steady-state flow) or the specified time period is completed (for unsteady flow).

In the present work, the 'time marching' approach has been used as a technique to obtain a steady-state solution as a limiting case. The rate of convergence to a steady state can be significantly affected by the coefficient of implicitization Π. The optimal value of Π is typically in the range of $0.5 \sim 1.0$ [5,15]. The algebraic equation sets are solved sequentially using the familiar tridiagonal matrix algorithm on a grid line, as illustrated by Patankar [26]. The convergence criterion adopted in the present work is that the non-dimensional total mass residuals for both the 3D continuity equation (7) and its depth-averaged form, Equation (13) be less than certain prescribed values. The transport equations for k, ϵ are solved in the same manner as the equation for the convection–diffusion process of Step 1.

4. BOUNDARY CONDITIONS

The water elevation $H+Z_b$ and hydrodynamic pressure p at all the boundaries, except at the outlet, are obtained by linear extrapolation from the values at the interior nodes. $H+Z_b$ at the outlet is prescribed, and p is set to be zero. The boundary conditions for the other dependent variables are given below.

At the inlet, the known boundary values for all the dependent variables ϕ (velocities, k, ϵ) are prescribed either from the experimental data or analytical profiles.

The outlet is placed in a downstream region where the equations can be parabolized so that the normal gradients can be set to zero for all dependent variables, i.e. $\partial\phi/dn = 0$. This may be somewhat inaccurate but stable, and the inaccuracy can be reduced by placing the outlet station sufficiently far downstream of the regions of interest [29]. In this study, the outlet station is located at least as far downstream as in the experiments. In the case of longitudinal velocity, however, the convective fluxes are corrected to satisfy overall continuity for the convergence consideration.

Near *the solid walls*, the variations of flow properties are very steep. To avoid the need for detailed calculations in the near wall region of low turbulent Reynolds number, the wall-function method is employed to simulate the wall effect and estimate the values of k, ϵ at the near wall nodes [23]. The wall-function method, which allows the use of a fairly coarse grid in the near wall region, is an economical way of modeling the turbulence.

In this work, the refined wall function is adopted because it is regarded as superior to the conventional log law wall function [30]. Variables are non-dimensionalized as $u^+ = u/U_*$, $y^+ = yU_*/\nu$, $k^+ = k/U_*^2$, $\epsilon^+ = \nu\epsilon/U_*^4$, where U_* is the friction velocity and y is the distance from the wall. In the refined wall function, the velocity normal to the wall is set to zero, while the near wall tangential velocities, calculated from the momentum equations, are related to the wall shear stress τ_w $(=\rho U_*^2)$ by a universal profile of mean velocity [31]. For smooth walls, this tangential velocity is given by

$$u^+ = 2.5\ln(1+0.2y^+) + 7.05\left(\frac{0.2y^+}{1+0.2y^+}\right)^2 + 2.5\left(\frac{0.2y^+}{1+0.2y^+}\right). \tag{37}$$

Equation (37) has been shows good agreement with experiments in all regions (viscous sublayer, buffer layer and fully turbulent region) [31]. The near wall k^+ and ϵ^+ are expressed by the analyses of experimental data:

$$\Theta = \frac{du^+}{dy^+} = \frac{1}{1+0.2y^+} + \frac{0.02(23.2-y^+)y^+}{(1+0.2y^+)^3}, \tag{38}$$

$$k^+ = \frac{0.75y^+}{11.6+y^+} + 0.2327y^{+2}\Theta^2, \qquad \epsilon^+ = f_\epsilon\Theta(1-\Theta), \tag{39}$$

$$f_\epsilon = 1 - 0.25\exp[-0.025(y^+-20)] + 0.2\exp[-0.05(y^+-10)^2]. \tag{40}$$

The performance of this refined wall function was demonstrated through a number of typical test cases [30] which showed that the predictions can be improved with the refined wall function where turbulence generation due to wall shear stress plays an important role.

At the free surface, the normal gradients of u, v, k are zero. By the definition of W in Equation (6), the boundary condition for W, w at the free surface ($\sigma \equiv 0$ or $z = H + Z_b$) are

$$W = 0; \qquad w = \frac{\partial H}{\partial t} + \frac{1}{J}\left(U\frac{\partial(H+Z_b)}{\partial\xi} + V\frac{\partial(H+Z_b)}{\partial\eta}\right). \tag{41}$$

An empirical relation for ϵ [23] is used to account for the damping effects on turbulence due to the presence of free surfaces. Without wind-induced shear at the free surface, the condition on ϵ is $\epsilon = 5.87k^{1.5}/H$.

5. NUMERICAL RESULTS AND DISCUSSION

The proposed model with Roe's scheme has been investigated by applying it to the following 2D/3D test cases: (1) laminar channel flow with a smooth expansion, (2) turbulent open channel flow in a 180° bend, and (3) turbulent open channel flow in a 60° channel bend with side overflow.

5.1. Case 1: channel flow with a smooth expansion (2D)

The first application is the laminar flow in a symmetric channel with a smooth expansion. This example has been used to compare various numerical models in the IAHR Workshop 1982 [32]. The numerical results were provided in terms of the vorticity Ω and the pressure p along the wall of the channel. The result of Cliffe *et al.* [32,33] on a 21×21 grid was considered as the reference solution. This problem has been used as a benchmarking case by a number of researchers, e.g. Giannakoglou *et al.* [34] and Sheu *et al.* [35].

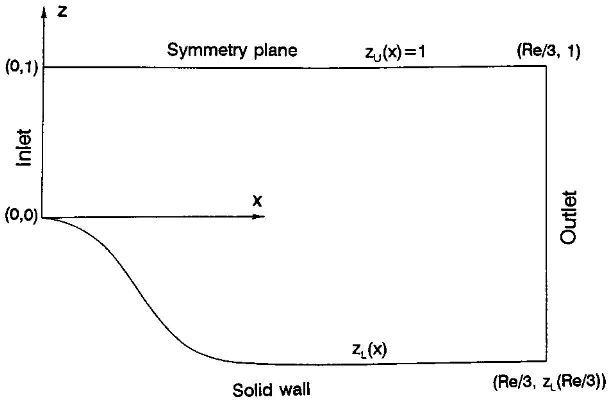

Figure 3. Geometry of smooth expansion channel.

One of the cases considered in the IAHR Workshop 1982 [32], the flow with $Re = 100$, was selected for the present study. The geometry of the 2D channel depends on the flow Reynolds number, as shown in Figure 3. The lower boundary (solid wall) of the channel is defined by

$$z_L(x) = \left[\tanh\left(2 - \frac{30x}{Re}\right) - \tanh(2)\right]/2, \qquad 0 \le x \le Re/3, \tag{42}$$

and the upper boundary, located at $z_U(x) = 1$, is a symmetry plane, which can be considered as a fixed free surface in the implementation of the present algorithm.

At the inlet, $x = 0$ and $0 \le z \le 1$, a fully developed Poiseuille flow condition is imposed as

$$u(z) = 3(z - z^2/2), \qquad w(z) = 0. \tag{43}$$

The outlet boundary conditions and the free surface (symmetry) boundary conditions have been stated in Section 4.

The present 3D model is simplified to apply to this 2D problem in the x–z-plane with a fixed free surface. Two non-uniform grids are used, i.e. a 21 × 21 grid (denoted as G1) and a finer 41 × 21 grid (denoted as G2). In the G1 grid, Δx increases linearly from 1.45 at the inlet to 1.75 at the outlet, and distribution of $\Delta\sigma$ is uniform; in the G2 grid, Δx varies linearly from 0.73 at the inlet to 0.9 at the outlet with uniform distribution of $\Delta\sigma$.

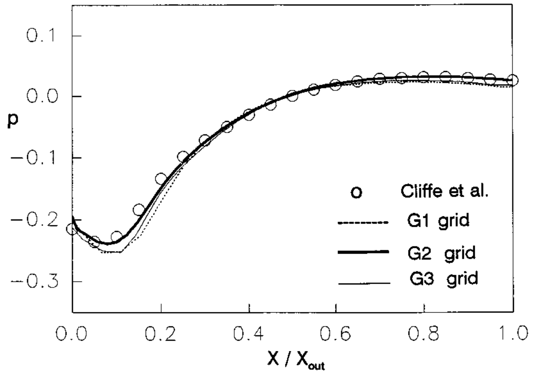

Figure 4. Wall pressure p distribution ($Re = 100$).

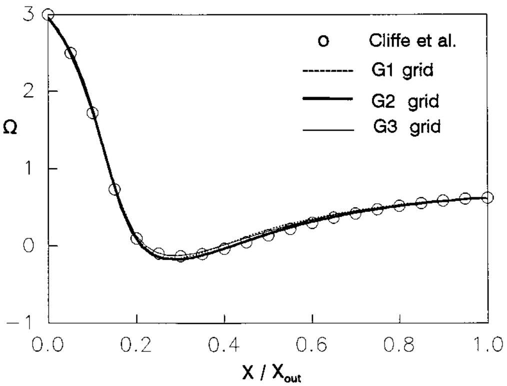

Figure 5. Wall vorticity Ω distribution ($Re = 100$).

Results of G1 and G2 grids in the form of pressure and vorticity distributions along the lower solid wall are presented in Figures 4 and 5, respectively, and compared with Cliffe *et al.*'s benchmark solutions [32,33]. The pressure distributions are normalized by setting the wall pressure to be zero at the half channel length $x = x_{\text{out}}/2$ [32]. The wall vorticity is obtained through a one-sided, second-order finite difference scheme using the interpolated velocity components over the grid nodes [34].

Simulations on the G1 grid show fair agreement with the benchmark results. Some discrepancy appears around the inlet and outlet regions for the pressure distribution (Figure 4), and near the inlet region ($x/x_{\text{out}} \leq 0.3$) for the vorticity distribution (Figure 5). With the grid refinement, the computations on the G2 grid illustrate excellent agreement with the solutions of Cliffe *et al.*

To further study the sensitivity of the outlet boundary conditions, a longer computational domain, $x_{\text{out}} = Re/2$, has been tested. A 31×21 grid is used with the same grid distribution as the 21×21 G1 grid within $x \leq Re/3$. Comparing with the solutions on the G1 grid of the shorter domain ($x_{\text{out}} = Re/3$), simulations of the wall vorticity are nearly identical for these two computational domains, while the wall pressure distributions are almost the same (the relative differences are within 0.4%), except at the last three nodes at the outlet, e.g. the relative difference at the third last node is $\approx 1.1\%$, and $\approx 2\%$ at the second last node. This comparison confirms that the outlet boundary conditions used here are adequate for the present problem in the shorter domain.

The above computations are performed in x–z-plane. This 2D problem can also be treated in x–y-plane. By introducing ξ-, η-co-ordinates, a quasi-orthogonal 21×21 grid (denoted as G3) is generated with grid concentrated near the upper and lower boundaries and in the high gradient region of the curved solid wall, i.e. around $x = Re/5$. The results for the vorticity from the present model are shown in Figure 5. Results with the G3 grid also exhibit some discrepancy with the benchmark solutions and the computations of the finer G2 grid. With the same grid density, solutions with the G3 grid provides some improvement over that with the G1 grid, because of the adopted distribution and the quasi-orthogonal property of the G3 grid.

5.2. Case 2: open channel flow with a 180° bend (3D)

In curved open channels, because of the non-uniform velocity distributions over the depth, centrifugal forces generate secondary currents and super-elevation of the water surface. Secondary currents produce a three-dimensional helical flow pattern and subsequently have a strong influence on the overall flow behaviour [36].

Experiments in an open channel with a 180° bend were conducted by De Vriend [37], and the depth-averaged velocity distributions and water surface profiles were reported. The channel cross section was rectangular, the centerline radius was 4.25 m, the inlet and outlet of the bend were connected to 6 m long straight reaches and the channel width was $B = 1.7$ m. The channel boundaries were hydraulically smooth. The flow discharge was $Q = 0.19$ m^3 s^{-1} with a constant downstream water depth $H_0 = 0.18$ m with Froude number = 0.47.

Computations are carried out with the 3D model for the same conditions as in the experiment, and the simulation results are compared with the available data of De Vriend [37]. A grid of $88 \times 26 \times 12$ in ξ-, η-, σ-directions, respectively, was set for the numerical calculations. Figure 6 shows the mesh in the x–y-plane. The lateral grid sizes are in the range of 0.02–0.1 m with grids concentrated near the wall regions, and the longitudinal grid sizes along the centerline are between 0.24–0.3 m. Uniform distribution of $\Delta\sigma$ is set in the vertical direction, and the implicitness coefficient and time step are taken as $\Pi = 0.85$, $\Delta t = 0.5$ s, respectively. After 1200 time steps, the solutions are regarded as steady-state when the mass residual for the 3D continuity equation (7) is less than 5.7×10^{-4} and that for the depth-averaged form, Equation (13), is less than 6×10^{-5}.

Figure 7 gives the depth-averaged velocity distributions at different locations. The agreement between the measurement and predictions is very good. Comparison of the water surface elevations are shown in Figure 8. The longitudinal distance from the inlet is normalized by the length at the centre of the bend and is shown as $\hat{S}$ in Figure 8. The deviation of the water surface is normalized as $\Delta H/H_0$. The results are compared at the centre line, at $B/10$ from the outer bank and $B/10$ from the inner bank. Generally, there is close agreement between the data and computations at the outer bank and centre, although there is some discrepancy along the middle part of the inner bank region. Figure 9 shows the secondary currents at various cross sections, i.e. generation of the secondary motion at 12.5° (Figure 9(a)), fully developed secondary current at 117.5° (Figure 9(b)), and near the exit of the bend (Figure 9(c)). It is notable that near the surface of the inner bank, the maximum secondary velocity appears below the free surface after the secondary currents developed (Figure 9(b,c)). A similar

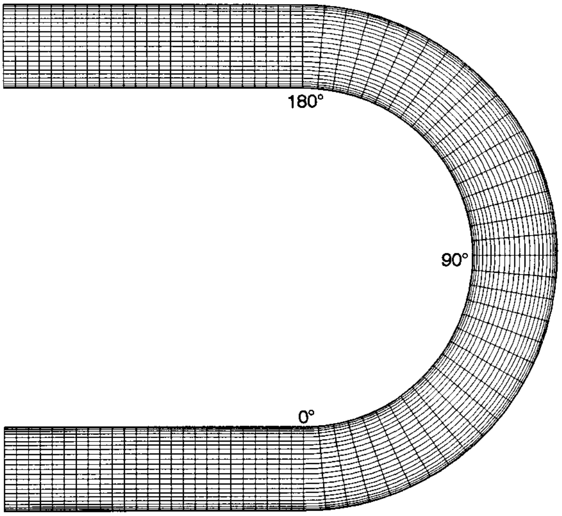

Figure 6. Grid system for 180° curved channel.

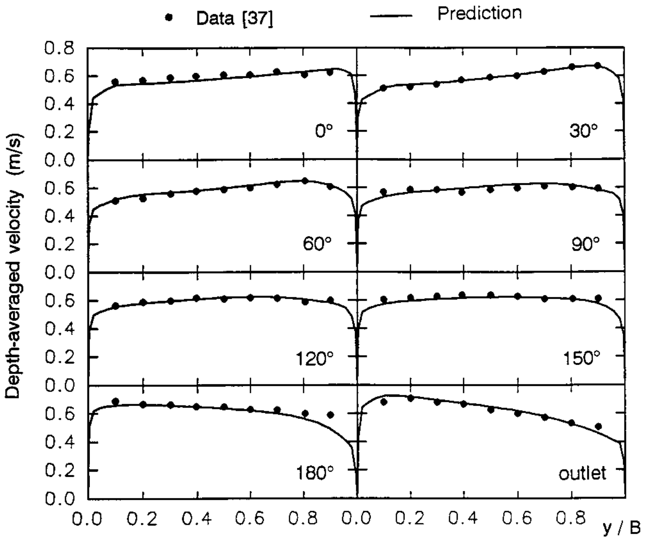

Figure 7. Depth-averaged velocity distribution at different stations.

phenomenon has be found in the laboratory study of a 270° curved open channel by Hicks *et al.* [38].

5.3. Case 3: flow in a 60° channel bend with a side overflow (3D)

A series of tests was conducted by Fare and Herbertson [39,40] for flows in a bent channel with a side overflow. The channel consisted of a 60° bend with a centerline radius of $r_m = 1.5$ m, as shown in Figure 10. Straight reaches were used to connect the inlet and outlet to the bend, with a length of 4 m for the straight upstream reach. A sluice gate was placed 0.8 m (1.6B) downstream of the end of the bend. The channel cross sections were rectangular with width $B = 0.5$ m and depth = 0.12 m. The channel boundaries were smooth and a Manning's coefficient n of 0.01 was reported. A gap was left in the outer wall of the bend between angles 25–35° to accommodate a flood relief channel of width $C_w = 0.3$ m with a side crest weir, as shown in Figure 10. The height of the side weir C_h was adjustable

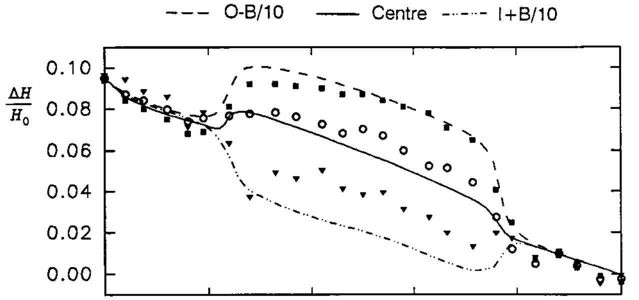

Figure 8. Water surface elevation along channel bend.

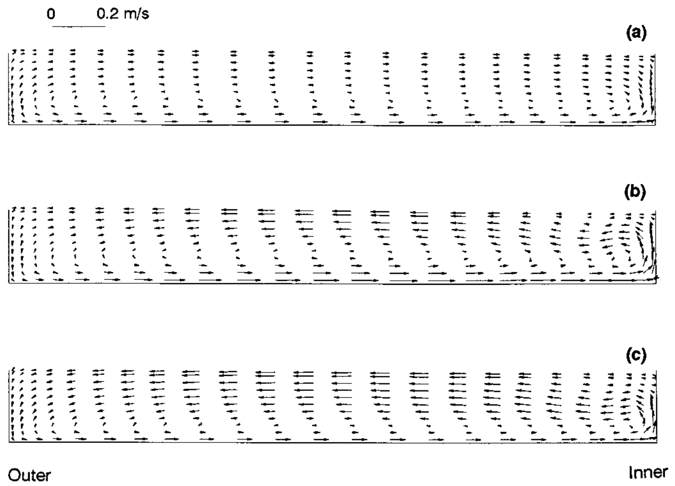

Figure 9. Secondary currents in the cross sections at (a) 12.5°, (b) 117.5° and (c) 177.5°.

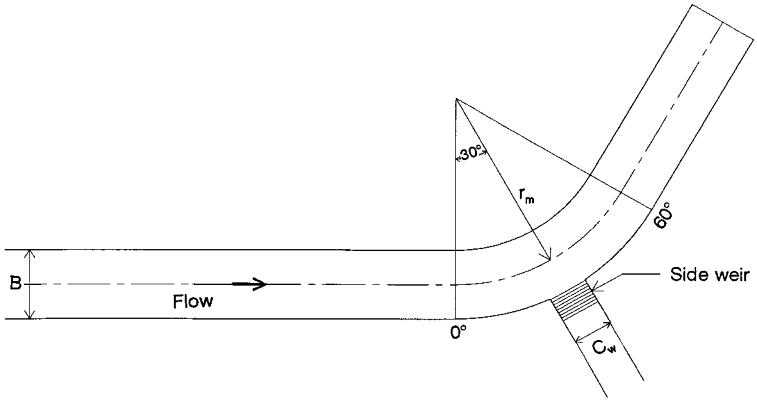

Figure 10. Configuration of 60° channel bend with a side overflow.

to control the side flow rate. The length of the side channel was 0.8 m, i.e. the side outlet was at $1.67C_w$ downstream of the side weir. The flow pattern was known to be fairly complex with strong 3D features [39,40]. In addition to the effects of curvature, the influence of the intersection affects the structure of the flow in the main channel along and downstream of the intersection. A total of 30 test runs were made. In this paper, two of these experiments, i.e.

Table I. Experimental test conditions [39,40]

Test run	Flow (Q) (m^3 s^{-1})	Flow over weir (Q_{fR}) (m^3 s^{-1})	Depth at entry to bend (H) (m)	Side weir depth (C_h) (m)
WF5	Water surface profile test			
	0.00794	0.00591	0.0768	0.025
A1–V1	Deviation angles and velocities test			
	0.00538	0.00224	0.0555	0.025

WF5 test and A1–V1 test, were selected as indicated in Table I. In the WF5 test, only the water elevation was measured, while in the A1–V1 test the velocity results were given in the main channel. Both tests are for high side overflow Q_{fR}.

The conditions used in the computations by the proposed 3D model were the same as those in the experiment, except for the lengths of the straight downstream reach and the side channel. To minimize the influence of the outlet boundaries on the upstream zones, the lengths of the straight downstream reach and the side channel are set to be 4.75 and 2.7 m respectively, which are much longer than those used in the experiments.

Two grid systems are used for simulations and comparison, i.e. a grid of $74 \times 48 \times 14$ (denoted by GA) and a finer grid of $117 \times 60 \times 14$ (denoted as GB) in ξ-, η-, σ-directions, respectively. Uniform distribution of σ is imposed in both grids. In the GA grid, 28 grid points are set in the lateral direction of the main channel with concentration near the side wall regions. The sizes of the control volumes in the physical plane are between 0.015 and 0.02 m (in the main channel) and 0.05–0.3 m in the lateral and longitudinal directions, respectively. Similarly, in the GB grid, 38 grids are non-uniformly distributed in the lateral direction of the main channel. The sizes of the control volumes in the physical plane vary between 0.01 and 0.0146 m (in the main channel) in the lateral direction and between 0.026 and 0.3 m in longitudinal direction. The other parameters are set as $\Pi = 0.85$ and $\Delta t = 0.1$ s. After 1100–1500 time steps, the solutions are regarded as steady-state when the mass residual for the 3D continuity equation (7) is $< 8.4 \times 10^{-4}$ and that for the depth-averaged form, Equation (13), is $< 2.1 \times 10^{-4}$.

For the flow in the side flood relief channel with a step height of C_h and significant change in the free surface, the grid lines in the (ξ, σ), (η, σ) planes do not properly represent the side weir and the σ-transform (4) may not be directly applicable. This is due to the severe non-orthogonal effect in the vertical plane, which can also cause poor convergence and accuracy. This difficulty can be practically overcome by assuming a moving 'false' bottom topography at the side weir depending on $H + Z_b$, and introducing the 'blocking' technique to deactivate the solid step zone as commonly adopted in the conventional finite volume method and finite difference method [26]. This treatment extends the capability of theσ-co-ordinate transformation. To ensure that the designed (ξ, σ), (η, σ) planes represent the step C_h, the imagined Z_b is expressed as

$$Z_b = \frac{C_h - (H + Z_b) \times (1 - \sigma_s)}{\sigma_s}, \tag{44}$$

where σ_s the designated σ-co-ordinate of the step. The imagined bed elevation Z_b is upgraded iteratively until convergence results in the final water elevation. This technique has also been used successfully in the simulation of the Lower Detroit River with natural irregular bathymetries [41].

5.3.1. Result for WF5 test water surface. The experiment has shown that along the intersection of the diversion, the flow was influenced by the formation of a stagnation zone at the inner bank that occupied almost half the width of both of the main channel and the side channel [39]. Basically, the results of free surface profiles on the two grids are very close, i.e. the relative differences are within 0.7%. Computations (on GB grid) of the water elevation distributions at various cross sections along the intersection are illustrated in Figure 11, which shows generally good agreement with the measurements. Figure 12 gives the zoomed x–y-plane view of the velocity vector fields around the intersection on GB grid (the vectors are plotted at every other row in the main channel in longitudinal direction for more clarity). The

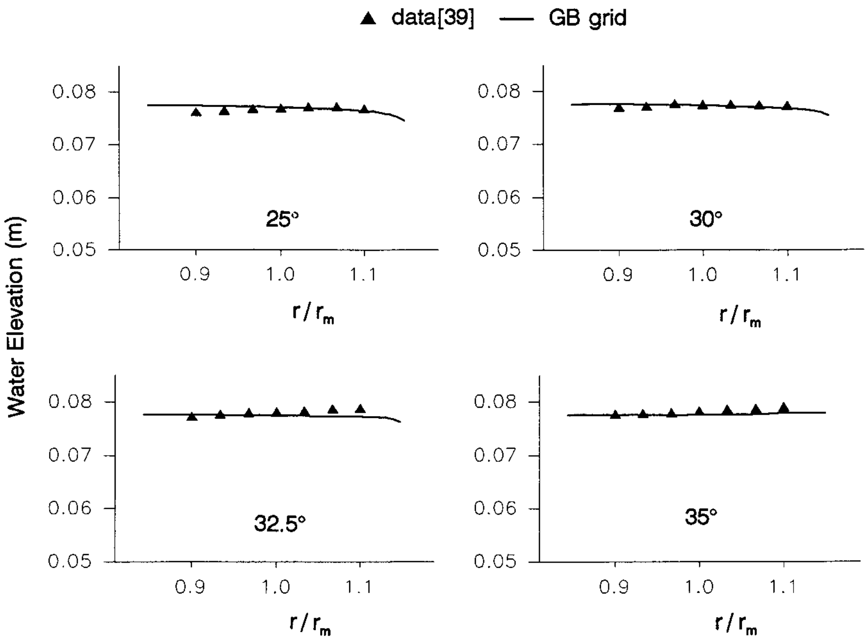

Figure 11. Comparison of water surface elevation for WF5 test.

stagnation and separation zones obtained from the simulation are qualitatively consistent with the observations.

5.3.2. Result for A1–V1 test velocity. Figure 13 shows the distribution of the depth-averaged velocity profiles at various cross sections, along with the measurements. Comparison of the solutions for two grid densities (GA and GB) indicates that grid convergence has been achieved with Roe's scheme. Solutions on the finer GB grid are only slightly better than those on the GA grid. The maximum relative difference of the simulated depth-averaged velocities is $\approx 4\%$. In Figure 13, solutions with the power law scheme on the finer GB grid are also presented. In comparison with the measurements, it can be seen that refinement of the grid distribution will not eliminate the impact of numerical diffusion caused by the first-order-accurate power law scheme in this simulation. It is notable that although Roe's scheme generates much improved solutions over the power law scheme, there still exists some discrepancy with the data, specifically near the recirculating zone. Since the standard k–ϵ turbulence model is used, the model does not adequately describe the non-isotropic structure of turbulence and tends to underestimate the size of recirculating zones where turbulent diffusion is important [23,42]. Higher-level turbulence models or other empirically modified k–ϵ models need to be incorporated to reduce this discrepancy [23,42].

Figure 14 illustrates the vertical profiles of the deviation angles θ_d° at three locations across the channel width, i.e. at $r/r_m = 0.9$, 1.0, 1.1. θ_d° was introduced to detect the relative strength of secondary current [40]. $\theta_d^\circ = 0$ means that the resultant velocity is aligned tangentially to the radius of curvature of the channel. $\theta_d^\circ > 0$ or $\theta_d^\circ < 0$ signify that the transverse velocity is directed towards the outer bank or inner bank of the channel. Due to the strong cross currents generated by the side overflow and the development of the separation zone along the inner bank, the velocities decrease gradually along the inner bank and the main flow shifts toward the outer bank along and downstream of the intersection [39,40]. Also, the experiment showed that along the intersection, there is no longer a reversal of the secondary current between the surface and bottom layers and θ_d° profiles are quite uniform vertically. Downstream of the intersection, the re-established transverse circulations are strongly distorted by the carry-over effect from upstream, i.e. the development of the bend secondary current is limited to 3/4 channel width leaving 1/4 inner width as a stagnation zone [40].

Results for θ_d° by the power law (on GB grid) and Roe's (on GA and GB grids) schemes are given in Figure 14. Similar trends can be observed as in Figure 13. In comparison with the experiments, it is observed that both schemes are reasonably accurate in the region outside of the separation zone, i.e. upstream of the intersection (0–25°), at the locations of $r/r_m > 0.95$ along the intersection (25–35°) and downstream of the intersection (35–50°). Near the recirculation region, the predicted curves by Roe's scheme give a much closer agreement with the measurements, i.e. the power law scheme significantly underpredicts the separation zone. The coarser (GA) grid in Roe's scheme is superior to the refined (GB) grid

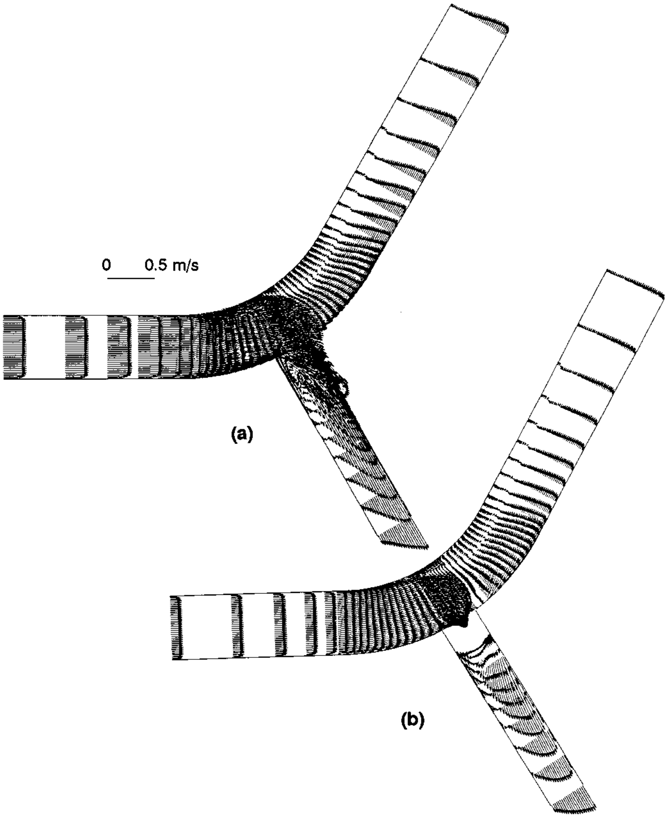

Figure 12. Velocity vector fields of WF5 test on GB grid (a) at surface (b) near bottom.

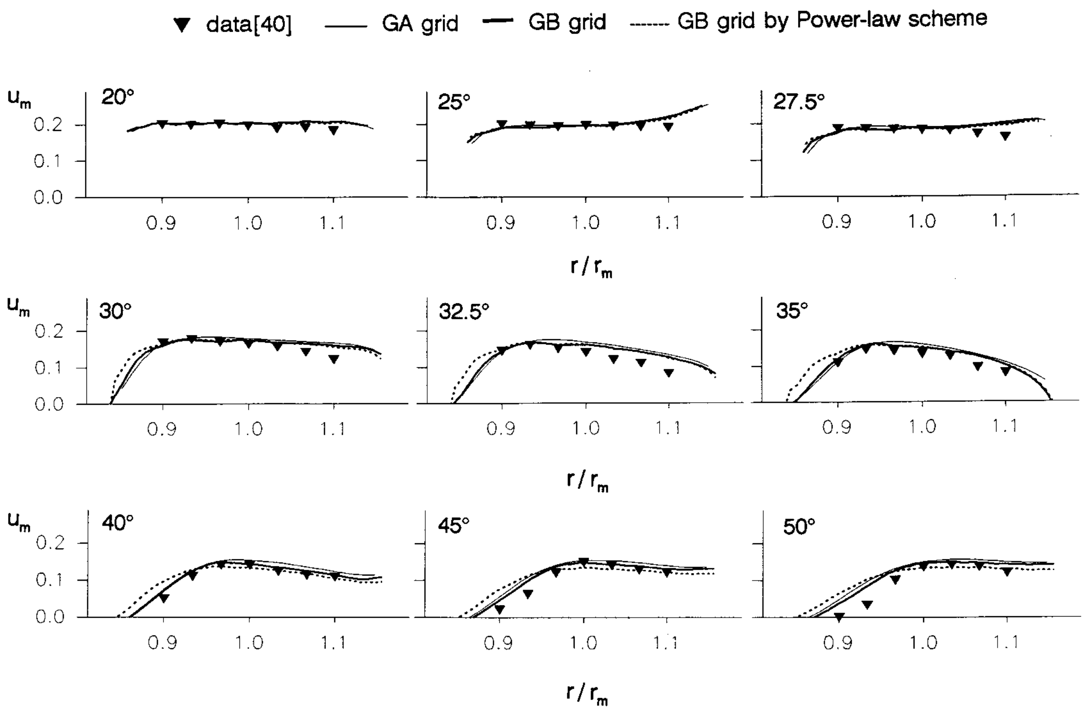

Figure 13. Comparison of depth-averaged velocity u_m (m s^{-1}) distribution for A1–V1 test.

in the power law scheme, even though computation with the power law scheme requires more CPU.

Figures 15 and 16 present the zoomed x–y-plane view of the velocity vector fields around the intersection on the GB grid for both schemes (the vectors are displayed at every other row in the main channel in longitudinal direction). Because of the nature of low numerical diffusion in the high-order upwind scheme, the flow patterns predicted by Roe's scheme show a larger separation zone throughout the depth, which is closer to the experiments.

Figure 17 gives the transverse velocity vector fields by Roe's scheme on the GB grid at three typical cross sections along the channel bend.

6. CONCLUSIONS

In this paper, a 3D hydrodynamic model for free surface flows has been developed, which solves the momentum equations, water depth and hydraulic dynamic pressure correction equations sequentially. A fractional three-step implicit algorithm has been described for flows in boundary-fitted curvilinear co-ordinates with a collocated grid system. A σ-co-ordinate transformation is adopted in the vertical z-direction. The model can handle an unprescribed, single-valued free surface and irregular, non-prismatic channel geometries. The second-order upwind scheme of Roe has been incorporated in the code for the discretization of the convective terms to minimize the numerical diffusion. This is the extension of the previous 2D model work [5,16] to 3D laminar or turbulent flows.

Three 2D and 3D test cases of steady free surface flows have been computed by the proposed unsteady fractional implicit algorithm, and results are compared with the benchmark solutions or experiments. Case 1 is a laminar flow with a smooth expansion. The other two cases are turbulent flows in curved open channels: case 2 is in a 180° bend and case 3 is a 60° bend with a side overflow.

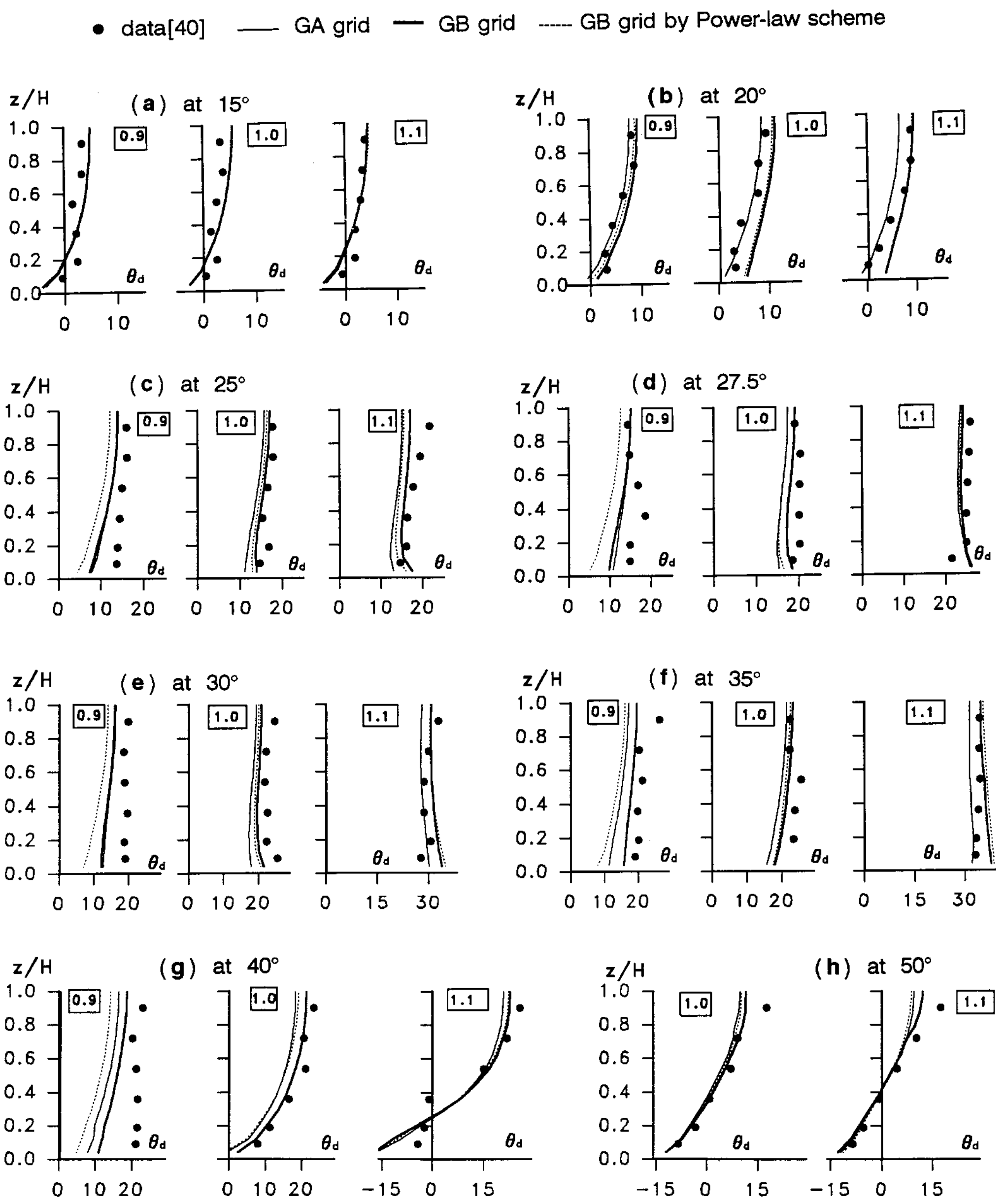

Figure 14. Comparison of vertical distribution of the deviation angles θ_d° for A1–V1 test at $r/r_m = 0.9, 1.0, 1.1$.

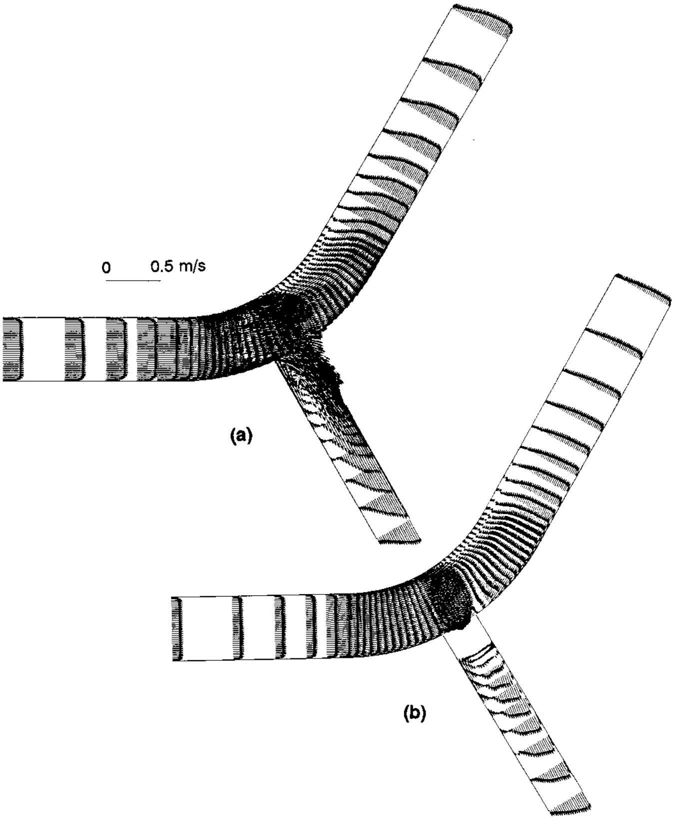

Figure 15. Velocity vector field of A1–V1 test on GB grid by Roe's scheme (a) at surface (b) near bottom.

In case 1, sensitivity analyses are performed on the grid density and distribution, and the extension of the outlet. Results are compared with the benchmark solutions, which shows that the computation is reliable. In case 2 and 3 of curved open channel flows, the predicted water surface profiles and velocity distributions agree reasonably well with the experiments.

The conventional σ-co-ordinate transformation in the vertical z-direction is restricted to the case of gradually varied bed topography. This shortfall is partly overcome by using an extension of the 'blocking' technique [26] that has been applied to represent the discontinuous step in case 3. Also in case 3, results of Roe's scheme are compared with those of the power law scheme, as well as available experimental data. The computational cost of improvements in accuracy of the predictions by the high-order scheme, i.e. Roe's scheme, is less than that associated with uses of grid refinement with the power law scheme, due to the effective reduction of the numerical diffusion for flows or certain regions of flows where the convection effect plays an important role in the momentum transport, e.g. flow separation zones.

Numerical results of the test cases demonstrate that, by taking advantage of the collocated grid arrangement and fractional step implicit algorithm, the present 3D hydrodynamic model is efficient, and can be successfully applied to problems in river engineering.

Further work is needed to incorporate higher level turbulence models or other empirically modified k–ϵ models to account for the non-isotropic turbulence effects.

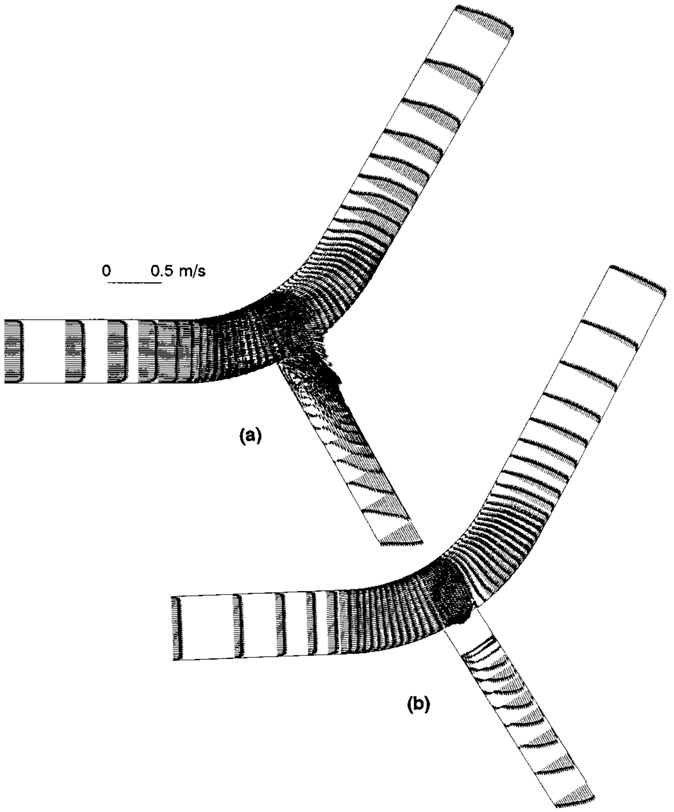

Figure 16. Velocity vector field of A1–V1 test on GB grid by the power law scheme (a) at surface (b) near bottom.

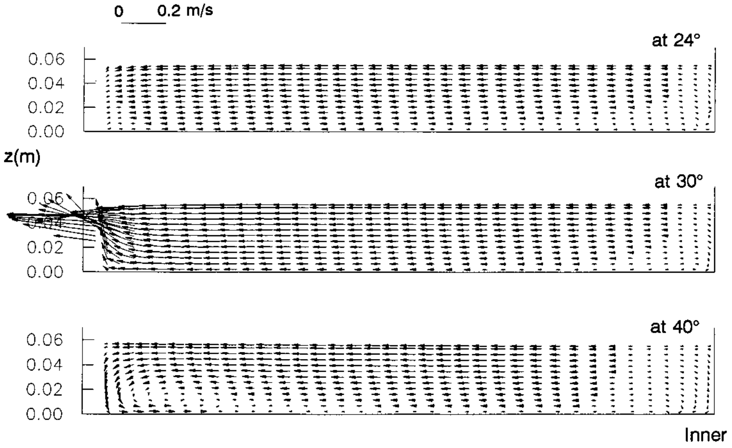

Figure 17. Cross sectional transverse current of A1–V1 test on GB grid.

ACKNOWLEDGMENTS

This research was supported by the Great Lakes Institute for Environmental Research, University of Windsor, Canada and the Natural Science and Engineering Research Council of Canada.

REFERENCES

1. J.F. Thompson, 'Numerical solution of flow problems using body-fitted coordinate systems', in W. Kollmann (ed.), *Computational Fluid Dynamics*, Hemisphere, New York, 1980.
2. W. Rodi, S. Majumdar and B. Schonung, 'Finite volume methods for two-dimensional incompressible flows with complex boundaries', *Comput. Methods Appl. Mech. Eng.*, **75**, 369–392 (1989).
3. K.M. Smith, W.K. Cope and S.P. Vanka, 'A multigrid procedure for three-dimensional flows on non-orthogonal collocated grids', *Int. J. Numer. Methods Fluids*, **17**, 887–904 (1993).
4. P. He and M. Salcudean, 'A numerical method for 3D viscous incompressible flows using non-orthogonal grids', *Int. J. Numer. Methods Fluids*, **18**, 449–469 (1994).
5. J. Ye, J.A. McCorquodale and R.M. Barron, 'A fractional two-step implicit algorithm with Roe's scheme in a curvilinear collocated grid', *Int. J. Numer. Methods Fluids*, submitted (1997).
6. M. Majumdar, 'Role of underrelaxation in momentum interpolation for calculation of flow with non-staggered grids', *Numer. Heat Transf.*, **13**, 125–132 (1988).
7. C.W. Hirt and B.D. Nichols, 'Volume of fluid (VOF) method for the dynamics of free boundaries', *J. Comput. Phys.*, **39**, 201–225 (1981).
8. J.J. McGuirk and W. Rodi, 'A depth-averaged mathematical model for the near field of side discharges into open channel flow', *J. Fluid Mech.*, **86**, 761–781 (1978).
9. F.H. Harlow and J.F. Welch, 'Numerical calculation of time-dependent viscous incompressible flow of fluid with free surface', *J. Phys. Fluids*, **8**, 2182 (1965).
10. R. Keunings, 'An algorithm for the simulation of transient viscoelastic flows with free surface', *J. Comput. Phys.*, **62**, 199 (1986).
11. S. Zhou and S. Zhang, 'Using HH-SIMPLE to solve bottom jet problem in open channel and shallow water for 3D situation', *Proc. 4th Asian Congress of Fluids Mechanics*, Hong Kong, 1989.
12. V. Casulli, 'Recent development in semi-implicit numerical methods for free surface hydrodynamics', *Proc. Advances in Hydro-Science and -Engineering*, Beijing, China, **V.2**, March 1995, pp. 2174–2181.
13. N.A. Phillips, 'A coordinate system having some special advantages for numerical forecasting', *J. Meteorol.*, **14**, 184–185 (1957).
14. G.S. Stelling and J.A.Th.M. Van Kester, 'On the approximation of horizontal gradients in sigma coordinates for bathymetry with steep bottom slopes', *Int. J. Numer. Methods Fluids*, **18**, 915–935 (1994).
15. J. Ye and G. Dou, 'Computation of incompressible fluid flows by an implicit fractional step scheme', *Proc. 2nd Inter. Conf. on Hydraulic and Environ. Modelling of Coastal, Estuarine and River Waters*, Bradford, England, 1992, pp. 529–539.
16. J. Ye and J.A. McCorquodale, 'Depth-averaged hydrodynamic model in curvilinear collocated grid', *J. Hydraul. Eng., ASCE*, **123**, 380–388 (1997).
17. P.L. Roe, 'Approximate Riemann solvers, parameter vectors, and difference schemes', *J. Comput. Phys.*, **43**, 357–372 (1981).
18. P.L. Roe, 'Some contributions to the modelling of discontinuous flows', *Proc. AMS/SIAM Seminar*, San Diego, 1983.
19. P.K. Sweby, 'High resolution schemes using flux limiters for hyperbolic conservation laws', *SIAM J. Numer. Anal.*, **21**, 995–1001 (1984).
20. P. Tamamidis and D.N. Assanis, 'Evaluation of various high-order-accuracy schemes with and without flux limiters', *Int. J. Numer. Methods Fluids*, **16**, 931–948 (1993).
21. D. Ambrosi, 'Approximation of shallow water equations by Roe's Riemann solver', *Int. J. Numer. Methods Fluids*, **20**, 157–168 (1995).
22. B.E. Launder and D.B. Spalding, 'The numerical computation of turbulent flows', *Comput. Methods Appl. Mech. Eng.*, **3**, 269–289 (1974).
23. W. Rodi, *Turbulence Models and their Application in Hydraulics—A State of the Art Review*, 2nd edn, IAHR, 1984.
24. J.P. Benque, J.A. Cunge, J. Feuillet, A. Hauguel and F.M. Holly, 'A new method for tidal current computation', *J. Waterw., Port, Coast. Ocean Div., ASCE*, **108**, 396–417 (1982).
25. N.N. Yanenko, *The Method of Fractional Steps*, Springer, Berlin, 1971.
26. S.V. Patankar, *Numerical Heat Transfer and Fluid Flow*, Hemisphere, New York, 1980.
27. B.P. Leonard and D.J. Dromond, 'Why you should not use Hybrid, Power-law or related exponential schemes for convective modelling—there are much better alternatives', *Int. J. Numer. Methods Fluids*, **20**, 421–442 (1995).
28. J.P. Van Doormaal and G.D. Raithby, 'Enhancements of the SIMPLE method for predicting incompressible fluid flows', *Numer. Heat Transf.*, **7**, 147–163 (1984).
29. L.E. Barton, 'Computation of dilute particulate laminar flow over a backward-facing step', *Int. J. Numer. Methods Fluids*, **22**, 211–221 (1996).
30. J. Ye, 'Improvement of wall function in turbulence modelling', *Proc. 5th Asian Congress of Fluid Mechanics*, Daejon, Korea, 1992.
31. G. Dou, 'General laws of turbulent flows', *Proc. 3rd Int. Symp. River Sedimentation*, Mississippi, USA, 1986, pp. 47–57.

32. M. Napolitano and P. Orlandi, ‘Laminar flow in a complex geometry: a comparison’, *Int. J. Numer. Methods Fluids*, **5**, 667–683 (1985).
33. K.A. Cliffe, C.P. Jackson and A.C. Greenfield, ‘Finite element solutions for flow in a symmetric channel with a smooth expansion’, *AERE-R.* 10608.
34. K.C. Giannakoglou and E.S. Politis, ‘Segregated algorithm for laminar incompressible flows’, *Int. J. Numer. Methods Fluids*, **21**, 1073–1077 (1995).
35. T.W.H. Sheu and S.-M. Lee, ‘A segregated solution algorithm for incompressible flows in general co-ordinates’, *Int. J. Numer. Methods Fluids*, **22**, 515–548 (1996).
36. H.H. Chang, *Fluvial Processes in River Engineering*, Krieger, Malabar, Florida, USA, 1992.
37. H.J. De Vriend, ‘A mathematical model of steady flow in curved shallow channels’, *J. Hydraul. Res.*, **15**, 37–53 (1977).
38. F.E. Hicks, Y.C. Jin, and P.M. Steffler, ‘Flow near sloped bank in curved channel’, *J. Hydraul. Eng.*, *ASCE*, **116**, 5570 (1990).
39. Y.R. Fares and J.G. Herbertson, ‘Partial cut-off of meander loops: a comparison of mathematical and physical model results’, in W.R. White (ed.), *Proc. Int. Conf. on River Flood Hydraulics*, Wallingford, UK, 1990, pp. 289–297.
40. Y.R. Fares and J.G. Herbertson, ‘Behaviour of flow in a channel bend with a side overflow (flood relief) channel’, *J. Hydraul. Res.*, **31**, 383–402 (1993).
41. J. Ye and J.A. McCorquodale, ‘Prediction of thermal discharge flows by a quasi-three-dimensional model’, *J. Hydraul. Res.*, *IAHR* (in press) (1998).
42. F. Durst and A.K. Rastogi, ‘Turbulent flow over two-dimensional fences’, in F. Durst, B.E. Launder, F.W. Schmit, J.H. Whitelaw (eds.), *Turbulent Shear Flow*, 2, edn, Springer, Berlin, 1980, pp. 218–232.